Available online at www.sciencedirect.com
SCIENCE DIRECT®
International Journal of Heat and Mass Transfer 48 (2005) 1267–1282
International Journal of HEAT and MASS TRANSFER
www.elsevier.com/locate/ijhmt

# Direct numerical simulation of turbulent flow in a vertical channel with buoyancy orthogonal to mean flow

O.A. El-Samni *, H.S. Yoon, H.H. Chun

*Advanced Ship Engineering Research Center (ASERC), Pusan National University, San 30 Chang Jeon Dong, Kum Jeong Gu, Pusan 609-735, South Korea*

Received 5 March 2004; received in revised form 4 October 2004
Available online 13 December 2004

**Abstract**

The effect of buoyancy on turbulent air flowing horizontally between two differentially heated vertical plates has been investigated using direct numerical simulation. Grashof number ranges between zero and $4.0 \times 10^6$ and the Boussinesq approximation is used in the buoyant term. In this particular configuration, the buoyancy forces result in skewed mean velocity profiles with non-zero anti-symmetric spanwise component $W$. The resulting flow has the features of three-dimensional turbulent boundary layer flows. In particular, suppression of the primary Reynolds stress in near-wall region is observed. Titled streaks with significant destruction of the associated vortical structures are highlighted. The induced mean spanwise strain enhances the turbulence intensities in the channel core. The effect of buoyancy on mean quantities and second-order statistics including Reynolds stress components and turbulent heat fluxes are presented and analyzed with detailed budgets of their transport equations which are believed to be helpful to testify and improve turbulence models incorporating buoyancy effect.


*Keywords:* Buoyancy; Vertical channel; Three-dimensional flows; DNS; Grashof number

## 1. Introduction

The buoyancy forces induced from density variation are relevant to many industrial and environmental applications such as heat exchangers, nuclear and chemical reactors, turbomachinery blades, and stratified atmospheric boundary layers. Such forces play significant role in the dynamics of mixed convective flows. Since the buoyancy forces are unidirectional, the alignment of the bounded walls with respect to them becomes the key role in characterizing the resulting flow regimes. The sole effect of buoyancy on wall bounded flows in the absence of the mean shear can be isolated and studied in details by simulating the turbulent natural convection in horizontal or vertical channel.

Phillips [1] simulated turbulent natural convection in vertical channel at Grashof numbers of 16200 and 45000 and showed that the turbulence originates from shear layer at the channel center. Few second-order statistics had shown high level of intensities at the channel centerline. Boudjemadi et al. [2] provided detailed databases for Reynolds stress components and turbulent heat fluxes aiming at assessment of second-moment closures

* Corresponding author. Tel.: +82 51 510 3670; fax: +82 51 581 3718.
*E-mail address:* elsamni@pusan.ac.kr (O.A. El-Samni).

0017-9310/$ - see front matter © 2004 Elsevier Ltd. All rights reserved.
doi:10.1016/j.ijheatmasstransfer.2004.10.014

**Nomenclature**

| | |
|---|---|
| $a_1$ | structure parameter; $\sqrt{(uv)^2+(wv)^2}/2k$ |
| $c_p$ | specific heat at constant pressure |
| $g_i$ | $i$th component of the gravitational acceleration |
| $Gr$ | Grashof number; $g\beta\Delta T(2\delta)^3/\nu^2$ |
| $k$ | turbulent kinetic energy |
| $l_{st}$ | streaks spacing |
| $p$ | pressure |
| $Pr_\tau$ | turbulent Prandtl number; $Pr_\tau=\frac{\nu_t}{\alpha_t}=\frac{-\overline{u'v'}}{\overline{v'\theta'}}\frac{\mathrm{d}\Theta/\mathrm{d}y}{\mathrm{d}U/\mathrm{d}y}$ |
| $q_w$ | wall heat flux |
| $Q$ | total mean velocity, $\sqrt{U^2+W^2}$ |
| $r_z$ | spanwise separation |
| $Re_\tau$ | Reynolds number, $Re_\tau=u_\tau\delta/\nu$ |
| $R_{u\theta}$ | streamwise cross-correlation of heat flux = $\frac{(\overline{u'\theta'}^2+\overline{w'\theta'}^2)^{1/2}}{\theta_{rms}(\overline{u^{2\prime}}+\overline{w^{2\prime}})^{1/2}}$ |
| $R_{ii}$ | two-point correlations |
| $t$ | time |
| $T$ | temperature in °C |
| $T_h$ | temperature of the hot wall |
| $T_c$ | temperature of the cold wall |
| $T_{ref}$ | reference temperature |
| $U,W$ | mean velocities in $x$- and $z$-directions |
| $V_b$ | reference buoyancy velocity, $g\beta\Delta T(2\delta)^2/\nu$ |
| $U_i,u_i$ | mean and instantaneous velocity component in $i$th direction |
| $u_\tau$ | friction velocity; $\sqrt{\tau_w/\rho}$ |
| $u_\tau^*$ | friction velocity estimated from the total mean velocity |
| $x,y,z$ | streamwise, wall-normal and spanwise directions |
| $\alpha$ | thermal diffusivity |
| $\beta$ | thermal expansion coefficient |
| $\Delta T$ | temperature difference ($T_h-T_c$) |
| $\delta$ | channel half width |
| $\delta_{ij}$ | Kronecker delta |
| $\gamma_m$ | cross-flow deviation angle, $\tan^{-1}$(W/U) |
| $\gamma_s$ | velocity gradient angle, $\tan^{-1}(\mathrm{d}W/\mathrm{d}y/\mathrm{d}U/\mathrm{d}y)$ |
| $\gamma_\tau$ | mean shear stress angle, $\tan^{-1}(-w'v'/-u'v')$ |
| $\lambda$ | thermal conductivity |
| $\nu$ | kinematic viscosity |
| $\Theta$ | mean temperature normalized by $\Delta T$ |
| $\theta$ | temperature normalized by $\Delta T$ |
| $\theta_\tau$ | friction temperature on the wall $q_w/\rho c_p u_\tau$ |
| $\rho$ | density |
| $\tau_w$ | wall shear stress |

*Subscripts and superscripts*

| | |
|---|---|
| rms | root mean square value of the fluctuating variable |
| + | normalized by wall variables; $u_\tau$,$\theta_\tau$, and $\nu$ on each wall |
| − | average over $x$–$z$ planes and time |
| ′ | fluctuating quantities |

for natural convection flows. They used two Grashof numbers of $1.41\times10^5$ and $7.6\times10^5$ in relatively small computational domain. By including the temperature variance and increasing Grashof number ten times ($7.62\times10^5$ and $7.1\times10^6$), Versteegh and Nieuwstadt [3] provided more detailed budgets and showed that their simulations are more reliable than those carried out by Boudjemadi et al. [2] considering computational the larger domain size and higher turbulence levels implemented in their study. Versteegh and Nieuwstadt [4] extended their earlier work [3] in order to investigate the scaling behaviors of several turbulence quantities aiming at proposing new wall functions. Surprisingly, they found that scaling behavior in inner and outer layer is quite difficult in natural convection despite the simplicity of problem. Wang et al. [5] observed large-scale spiral coherent structures at $Gr=7.62\times10^5$ which was used by Versteegh and Nieuwstadt [3]. The length scale of the spiral structures was found to be comparable to the channel width and their life-time was more than two orders of magnitude larger than the small scale structures of turbulence.

Concerning horizontal channels, Wörner and Grötzbach [6] performed DNS with two different thermal conditions, namely, the classical Rayleigh–Bénard channel heated from below, and the internally generated natural convection. Their simulation was performed at $Gr$ of $8.87\times10^5$. They emphasized on the role played by the intermittence of thermal plumes on the transport of turbulent kinetic energy. Domaradzki and Metcalfe [7] performed DNS of Rayleigh–Bénard convection where $Gr$ ranges between $5.0\times10^4$ and $8.88\times10^5$. They found that the pressure-diffusion term is responsible for redistributing the kinetic energy inside the convective boundary layer in contrary to the assumptions used in some turbulence models.

Combined forced and natural convection has attracted little attention due to the difficulties associated with the buoyancy and mean shear interactions. Kasagi and Nishimura [8] studied the turbulent convection in vertical channel where the buoyancy is aligned in the streamwise direction and the flow is upward. The resulting flow showed distinctive behaviors near each wall due to the aiding and opposing effects. Enhancement of Rey-

nolds stress components and wall normal turbulent heat flux was observed in the aiding flow, whereas they were suppressed in the opposing flow. Iida and Kasagi [9] and Iida et al. [10] studied the buoyancy effect in horizontal turbulent channel flow of unstably and stably stratified flows, respectively. In unstable stratification [9], thermal plumes emerged from the near wall region were observed to affect the transport mechanisms in the near-wall region through the pressure diffusion and turbulent diffusion terms. Such thermal plumes work to concentrate the coherent streamwise vortices at the regions from which they emerged and therefore they change slightly the low and high speed streaks. On the other hand, stable stratification shows suppression of turbulence intensities and dominance of internal gravity waves. The streamwise vortices are concentrated between the internal gravity waves in longitudinally and vertically elongated regions.

It has been recognized that buoyant flows has attracted relatively little effort in turbulence modeling improvement due to the scare experimental and numerical data available. Most of the developments done so far were based on DNSs of turbulent natural convection due to its simplicity. Readers can refer to the recent articles of Dol et al. [11], Sommer and So [12], Girimaji and Balachandar [13] and Dol and Hanjalić [14], who used DNS databases generated from Rayleigh–Bénard and vertical natural convection summarized above in the assessment of turbulence models.

The objective of the present study is to explore the interaction between the buoyancy forces with the mean shear when the former become perpendicular to the mean flow direction. As shown in Fig. 1, the buoyancy forces would induce lateral motion causing the mean flow to be skewed with non-zero anti-symmetric spanwise mean velocity component $W$. The resulting flow becomes more complex due to the three-dimensionality and the present study provides a new benchmark for turbulence modeler to testify their models in predicting three-dimensional flows. Moreover, predicting the thermal field is to be challenging due to the non-linear interaction between the thermal and flow fields through the buoyancy production terms which are basically functions of the temperature variances and turbulent heat fluxes. The effect of buoyancy is tackled while changing $Gr$ and observing the changes in mean quantities, Reynolds stresses, temperature RMS and turbulent heat fluxes. Three-dimensional characteristics of the resulting flow are to be presented along with the budgets of the transport equations of Reynolds stresses and turbulent heat fluxes. Instantaneous flow and thermal fields are visualized to shed the light into the changes in flow structures in this class of buoyant flows.

## 2. Computational details

The buoyancy vector is set perpendicular to the mean flow direction and the mean temperature gradient vector as shown in Fig. 1. One wall is heated and the other is cooled giving sufficient temperature difference to consider the buoyancy effect. In non-buoyant flows, Tiselj et al. [15] and Seki et al. [16] have confirmed the similarity between mechanisms of momentum and heat transfer in the wall region at the isothermal wall boundary conditions. Hence, the present study applies the isothermal boundary conditions with zero temperature fluctuations at both walls in order to investigate the effect of buoyancy on momentum and heat transfer mechanisms. No-slip and no-penetration conditions corresponding to both walls are enforced. The fluid properties are also assumed to be constant, except for the fluid density in the buoyancy term, which follows the Boussinesq approximation. Governing equations describing the instantaneous flow and thermal fields in the present study are the unsteady three-dimensional continuity, momentum and energy equations:

$$\frac{\partial u_i}{\partial x_i} = 0, \tag{1}$$

$$\frac{\partial u_i}{\partial t} + u_j \frac{\partial u_i}{\partial x_j} = -\frac{1}{\rho}\frac{\partial p}{\partial x_i} + \nu \frac{\partial^2 u_i}{\partial x_j^2} + g_i \delta_{i3} \beta (T - T_{\mathrm{ref}}), \tag{2}$$

$$\frac{\partial T}{\partial t} + u_j \frac{\partial T}{\partial x_j} = \alpha \frac{\partial^2 T}{\partial x_j^2}. \tag{3}$$

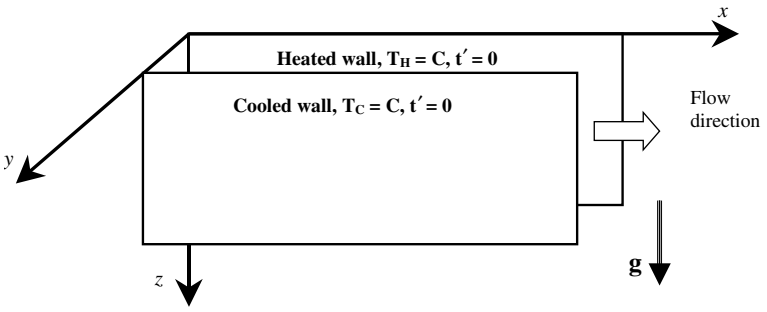


Fig. 1. Schematic representation of the vertical channel.

The reference temperature $T_{ref}$ in the present study is assumed to be the mean bulk temperature, which is updated every time step. The variables in the above equations are normalized by the channel half depth $\delta$, friction velocity $u_\tau$ and temperature difference between the two walls $\Delta T$. The normalization results in two dimensionless parameters; the friction Reynolds number $Re_\tau$ and Grashof number $Gr$. Three Grashof numbers of $9.6\times10^5$, $1.92\times10^6$ and $4.0\times10^6$ have been investigated. The range covers the previously studied forced convection DNS for the sake of comparison. The driving pressure gradient is adjusted to keep constant mass flow rate in the $x$-direction in all simulations. The computational domain has the dimensions $5\pi\delta\times2\delta\times2\pi\delta$ in $x$-, $y$- and $z$-directions, respectively. Those dimensions have been shown to be sufficient to capture the large thermals and plumes in wall bounded flows. Two-point correlations have shown decaying values at separations less than the channel length in the streamwise and spanwise directions, which indicates the suitability of the present domain size to capture large-scale structures. The flow is assumed fully developed so that the periodic boundary conditions are simply assigned in the mean flow ($x$) direction as well as the vertical or spanwise ($z$) direction.

Pseudospectral code is used in the simulations of the channel flow. It eliminates the pressure by transforming the Navier–Stokes equations to the vorticity-normal velocity formulation. This technique was originally proposed by Kim et al. [17] in their study of plane channel flow. Fourier series have been used for expanding the resolved variables in the homogenous directions while Chebyshev polynomial expansion is employed in the wall-normal direction. The computations are carried out at $128\times129\times128$ in $x$-, $y$- and $z$-directions, respectively and the 3/2 rule has been used to remove the aliasing errors.

The code was verified with the inclusion of rotational effects with different orientations [18] and tested with the buoyancy aligned in the streamwise direction and gave excellent agreement with Kasagi and Nishimura [8] data for the same Grashof number. For the present study, the results of the highest $Gr$ have been compared with further computations resulted from finer grids of 192 in each direction and have shown good matching with deviation less than 1.5% in the second-order statistics. Hence, the present resolution can be considered satisfactorily and reasonable within the specified range of $Gr$. The time advancement uses the Crank–Nicolson scheme for the diffusion terms and the second-order Adams–Bashforth scheme for the non-linear and buoyancy terms. The time step is set to 0.03 $\nu/u_\tau^2$ to keep the CFL number below 0.3. After reaching fully developed state, plane averages over $x$–$z$ planes and time as well have been accumulated for non-dimensional time interval of 2700 $\nu/u_\tau^2$ which is quite longer than the periods used in generating databases in the other DNS simulations of buoyant channel flows.

## 3. Results and discussions

### 3.1. Mean quantities

The present configuration and thermal boundary conditions have induced the anti-symmetric profiles of mean spanwise velocity $W$ due to the opposite effect of buoyancy forces near each wall. The two components of the mean velocity are plotted in global units for the different $Gr$ as shown in Fig. 2(a). Although the streamwise mean velocity shows little flatten profiles in the channel core, the spanwise component is rapidly increasing showing stronger anti-symmetry trend as $Gr$ increases. The profiles of $W$ seem similar to those induced in natural convection in vertical channels [1] and [2] under the same thermal boundary conditions. It can be clearly observed that the newly generated spanwise gradient $dW/dy$ increases in the channel core region and extends to nearly two thirds around the centerline of the channel. Accordingly, this strain will play a key role in enhancing the turbulent activities in the channel core.

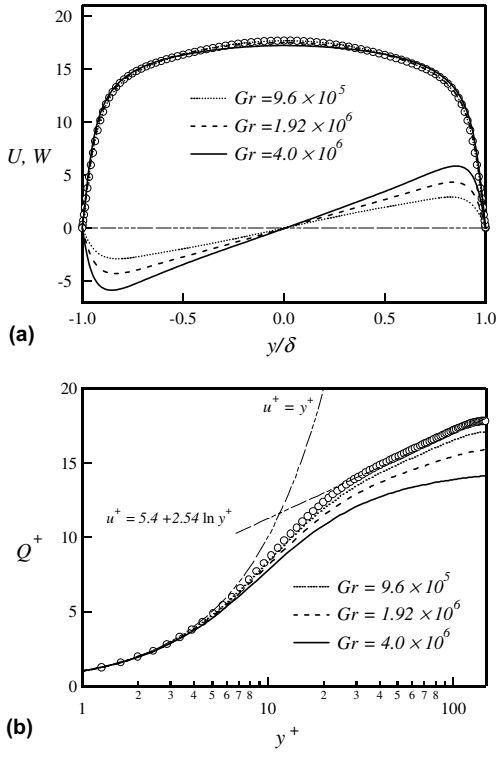


Fig. 2. Mean velocity profiles: (a) streamwise and spanwise components in global units, (b) the total mean velocity in wall units. Circles refer to plane channel of Iida et al. [10].

It is worth mentioning that the increase in $W$ has not associated with similar change in $U$ in near wall region which indicates that the flow is not collateral in contrast to the three-dimensional turbulent boundary layer flows (3DTBL) initiated by applying strong spanwise pressure gradient studied by Compton and Eaton [19].

Profiles of the total mean velocity $Q$ normalized by $u_\tau^*$ are plotted in Fig. 2(b) along with the non-buoyant case. Although the profiles are fitted well in the viscous sublayer, they deviate considerably in the buffer layer and in the outer region with increasing $Gr$, which indicates the difficulty of scaling the mean total velocity with the inner values. However, the log-law is preserved with decreasing slopes as $Gr$ increases, which implies the thinning of boundary layer thickness and the increase of the skin friction. Although it is not shown here, the profiles of $W$ do not show consistent scaling with either inner values or with the reference buoyancy velocity scale $V_b$ in according to Versteegh and Nieuwstadt [4] who addressed the difficulty to scale the velocities in turbulent natural convection.

The mean temperature profiles for different $Gr$ compared with the non-buoyant case scaled by $\Delta T$ and $\theta_\tau$ are plotted in Fig. 3(a) and (b), respectively. The asymmetric trend becomes stronger with increasing $Gr$ where the mean temperature gradient becomes larger in near-wall region and decreases in the channel core region. Higher rates of heat transfer and enhanced mixing in the channel core are attained with increasing $Gr$. Similar to the total velocity profiles shown in Fig. 2(b), the temperature profiles scaled with the inner values fit well in the viscous sublayer and show also deviation in the log-law region as $Gr$ increases. It is worth mentioning that the logarithmic region diminishes in the velocity and temperature profiles of both the unstable stratification case [9], and the aiding flow of streamwise oriented buoyant flow case [8]. This confirms the difficulty arising in modeling buoyant flows especially when the bounding walls are changing with respect to the gravity vector.

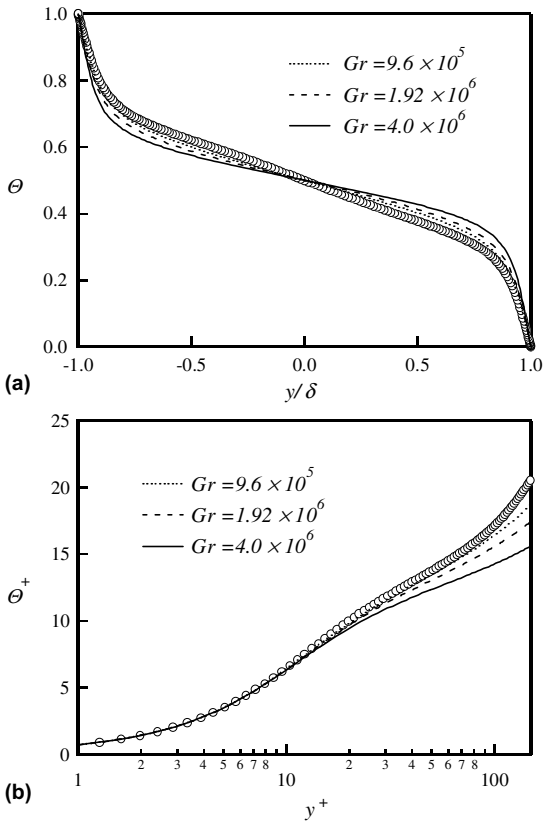


Fig. 3. Mean temperature profiles: (a) in global units, (b) in wall units. Circles refer to the non-buoyant case of Iida et al. [10].

### 3.2. Second-order statistics

RMSs of the Reynolds normal stresses normalized by $u_\tau^*$ are show in Fig. 4. It can be seen obviously that only

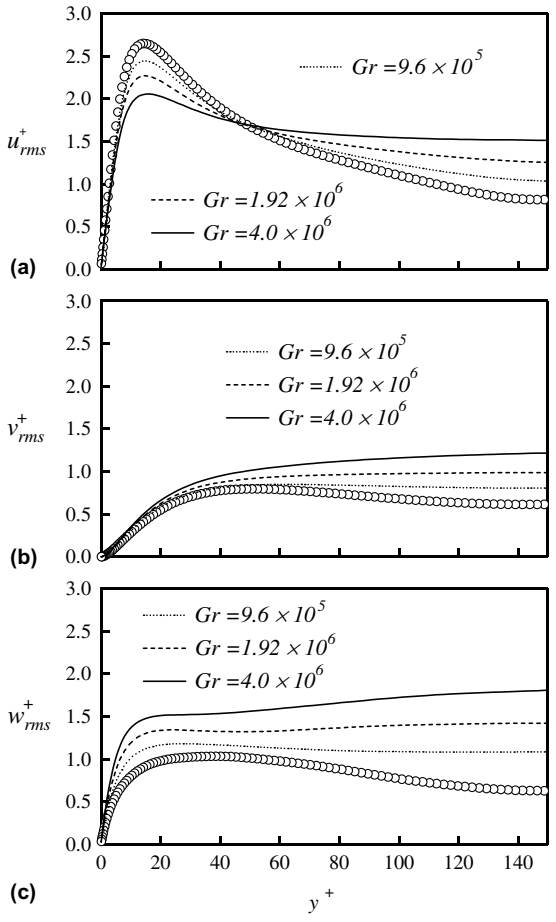


Fig. 4. RMS of normal Reynolds stress components plotted in wall units. (a) $u_{\rm rms}$, (b) $v_{\rm rms}$, and (c) $w_{\rm rms}$. Circles refer to plane channel flow of Iida et al. [10].

$u^+_{rms}$ decreases significantly in the buffer layer at $y^+ < 50$ with increasing $Gr$ as shown in Fig. 4(a). The other lateral components $v^+_{rms}$ and $w^+_{rms}$ increase especially $w^+_{rms}$ which shows rapid increase in near-wall region. In log-law region, the three components increase with the increasing $Gr$ and it is easily observed that both $v^+_{rms}$ and $w^+_{rms}$ have their peaks at the channel centerline at the highest $Gr$. The augmentation of $v^+_{rms}$ and $w^+_{rms}$ appeared along the whole channel depth indicates the activation of cross-stream eddies generated and evolved from the thermal plumes emerged from each wall. Such plumes penetrate each other due to the opposite spanwise motion of fluid layers near each wall as will be shown in the images of cross-stream flow visualizations.

Due to the three-dimensionality induced by the skewed mean flow, non-zero off-diagonal Reynolds stresses have been generated. In Fig. 5, the three stresses normalized by the inner values are plotted. The primary Reynolds shear stress $-\overline{u'^+v'^+}$ shows considerable reduction approaching 15 % at the highest $Gr$ in the buffer layer similar to the 3DTBL flows resulted from applying spanwise pressure gradient, deduced experimentally by Eaton and his co-workers [19] and [20] and numerically by Moin et al. [21]. The reduction can be attributed to the skewing of the mean flow towards to the spanwise direction and the substantial reduction of $u^+_{rms}$ in the buffer layer shown in Fig. 4(a). The non-zero mean strain $dW/dy$ generates the other off-diagonal Reynolds stresses which are typically zeros in 2DTBL. In Fig. 5, the secondary shear stress $\overline{v'^+w'^+}$ shows symmetric profiles with a maximum peak at the channel centerline due to the higher gradient of $W$ attained there. The peak of $\overline{v'^+w'^+}$ in near wall region at $y^+ < 20$, $\overline{v'^+w'^+}$ seems stationary and does not change with increasing $Gr$ due to energy transfer by the pressure diffusion from near-wall region to the outer layer as will be shown later. The magnitude of the third stress $\overline{u'^+w'^+}$ is comparable to the other two stresses. The stress is anti-symmetric around the channel centerline and it changes its sign within each half of the channel at $y$ -positions where both $dW^+/dy^+$ and $\overline{v'^+w'^+}$ change their signs. Further explanations to the trends of the Reynolds stresses can be extracted from the budgets of the transport equations relevant to each stress component.

In Fig. 6, with increasing $Gr$, the turbulent kinetic energy decreases substantially in the buffer layer where $\overline{u'^+u'^+}$ attains its maximum reduction as shown in Fig. 4(a). Although $\overline{v'^+v'^+}$ and $\overline{w'^+w'^+}$ increase in the buffer layer but they do not overwhelm the significant reduction of $\overline{u'^+u'^+}$. In the outer layer, continuous increase of $k^+$ is clearly observed with increasing $Gr$. At the highest $Gr$, another local peak of $k^+$ appears at the channel centerline as a consequence of increasing the three normal Reynolds stresses in the core region.

In order to testify the three dimensional characteristics of the flow, the structure parameter $a_1$, defined as the ratio of the total shear stress magnitude to twice the turbulent kinetic energy, is presented in Fig. 7 for

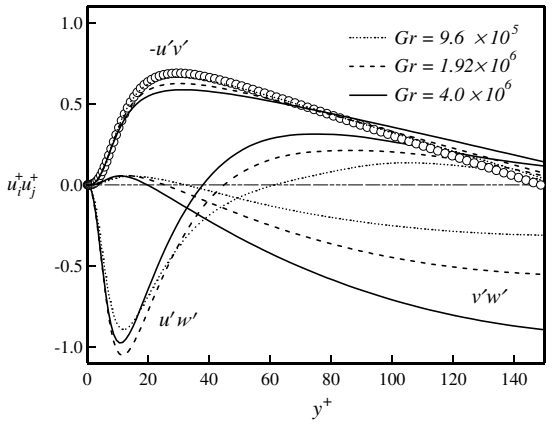


Fig. 5. Off-diagonal Reynolds shear stress components. Circles refer to plane channel flow of Iida et al. [10].

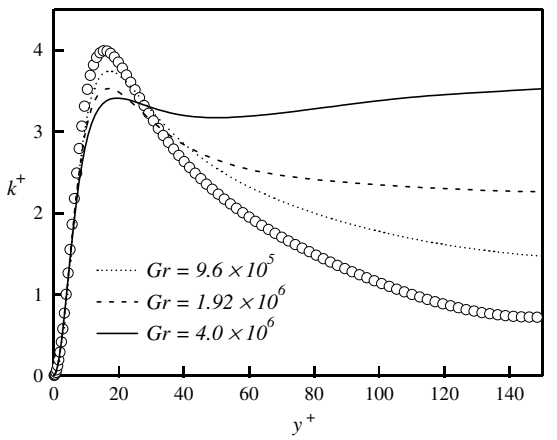


Fig. 6. Turbulent kinetic energy. Circles refer to plane channel flow of Iida et al. [10].

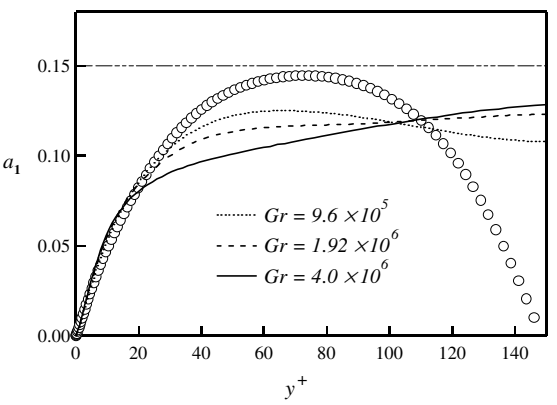


Fig. 7. The structure parameter $a_1$. Circles refer to plane channel flow of Iida et al. [10].

the three Grashof numbers. Similar to most of 3DTBL flows, in the range of $20 > y^+ > 100$, $a_1$ is lower than 0.15, the value observed in 2DTBL flows. At $y^+ > 100$, with increasing $Gr$, $a_1$ increases due to the considerable increase of the secondary shear stress $\overline{v'^+w'^+}$, shown in Fig. 5, and approaches 0.15 at the channel centerline for the highest $Gr$.

Another justification for the flow three-dimensionality is to compare the directions of the shear stress vector (shear angle $\gamma_\tau$) and that of the velocity gradient vector (strain angle $\gamma_s$). For this purpose, the flow angles profiles are presented in Fig. 8. In all the studied cases, strain angle $\gamma_s$ leads the shear angle $\gamma_\tau$ in near-wall region whereas $\gamma_s$ lags $\gamma_\tau$ further away from the wall. Concerning turbulence modeling, such flow angles can be a measure of the anisotropy of the eddy viscosity. If $(\gamma_s - \gamma_\tau) \sim 0$, the assumption of the isotropic eddy viscosity would be valid, which means that the ratio between the spanwise eddy viscosity $-w'v'/(\mathrm{d}W/\mathrm{d}y)$ to the streamwise eddy viscosity $-u'v'/(\mathrm{d}U/\mathrm{d}y)$ equals one. The lag angle $(\gamma_s - \gamma_\tau)$ is observed to be around 13° at the outer edge of the buffer layer at $Gr = 9.6 \times 10^5$ and $1.92 \times 10^6$, as shown in Fig. 8(a) and (b). At the highest $Gr$, it approaches 20° in near-wall region as shown in Fig. 8(c). The isotropy can be observed only in very limited region of $y^+ > 120$ only at $Gr = 1.92 \times 10^6$. The large lag angles observed in the present study makes the assumption of isotropy eddy viscosity questionable.

### 3.3. Temperature statistics

RMS of temperature fluctuations normalized by the friction temperature $\theta_\tau$ is shown in Fig. 9(a) for different $Gr$. In the viscous sublayer, the profiles of $\theta^+_{\mathrm{rms}}$ are fitted well when scaled with $\theta_\tau$ rather than $\Delta T$. In the outer layer, $\theta^+_{\mathrm{rms}}$ decreases with increasing $Gr$ due to the effective mixing of the core region which results in remarkable reduction of the mean temperature gradient as shown in Fig. 3. The peak of $\theta^+_{\mathrm{rms}}$ observed at the channel center in non-buoyant flows with the walls kept at constant temperature difference, disappears when the $Gr$ increases. Although it is not shown here, $\theta^+_{\mathrm{rms}}$ scaled with $\Delta T$ shows larger RMS in the viscous sublayer and the buffer layer followed by much suppression in the outer layer while increasing $Gr$. This reflects the difficulty in scaling the temperature in accordance with the conclusion of Versteegh and Nieuwstadt [4] in turbulent natural convection.

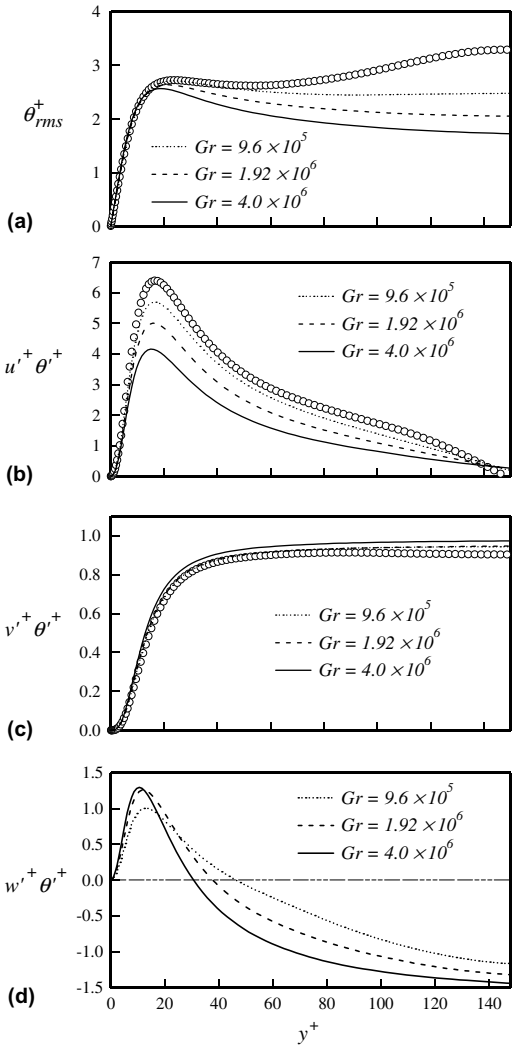


Fig. 9. Thermal statistics: (a) RMS of temperature fluctuations, turbulent heat fluxes, (b) $\overline{u'^+\theta'^+}$, (c) $\overline{v'^+\theta'^+}$ and (d) $\overline{w'^+\theta'^+}$. Circles refer to plane channel flow of Iida et al. [10].

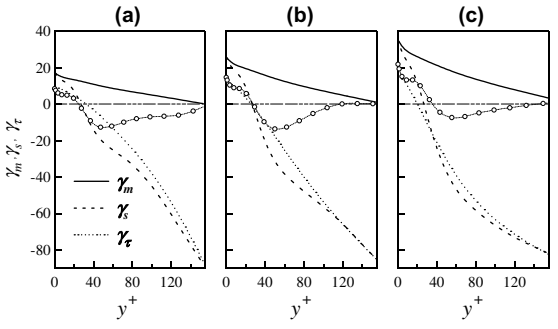


Fig. 8. Flow angles: (a) $Gr = 9.6 \times 10^5$, (b) $Gr = 1.92 \times 10^6$, (c) $Gr = 4.0 \times 10^6$. Circles refer to lag angle $(\gamma_s - \gamma_\tau)$.

The three components of turbulent heat flux are plotted in Fig. 9(b)–(d) for the three Grashof numbers. The streamwise component $\overline{u'^+\theta'^+}$ is obviously decreasing in buffer and outer layers due to the substantial decrease of

$u^+_{rms}$ in the buffer layer shown in Fig. 4(a) and to the continuous decrease of $\theta^+_{rms}$ in the outer layer as shown in Fig. 9(a). With increasing $Gr$, the wall normal turbulent heat flux $\overline{v'^+\theta'^+}$, shown in Fig. 9(c), is slightly enhanced over most of the channel in accordance with the considerable increase in the wall normal velocity fluctuations shown previously in Fig. 4(b). The newly generated spanwise turbulent heat flux $\overline{w'^+\theta'^+}$ is symmetric at the channel centerline with a peak near the wall of opposite sign to the minima at the centerline, as shown in Fig. 9(d), in accordance with the changes of $dW/dy$ over the channel width. The peak of $\overline{w'^+\theta'^+}$ in near wall region, seems unchanged at $Gr = 1.92\times10^6$ and $4.0\times10^6$ and the minima in the core region are continuously increasing with increasing $Gr$.

The turbulent Prandtl number, defined by as the ratio of the eddy diffusivity for momentum to the eddy diffusivity for heat, is plotted in Fig. 10 in comparison with other buoyant channel flows. As the wall is approached, $Pr_\tau$ tends to be 1.0 for air [16]. However, in all the presented cases, the asymptotic values of $Pr_\tau$ slightly increase with increasing $Gr$ where they approach 1.04, 1.08 and 1.1 for $Gr$ of $9.6\times10^5$, $1.92\times10^6$ and $4.0\times10^6$, respectively. For $y^+ > 10$, the profiles of $Pr_\tau$ deviate sharply from the non-buoyant profile and do not show the second peak which appeared in non-buoyant flows around $y^+ \approx 50$. The typical value of $Pr_\tau = 0.9$, which is usually used in turbulence modeling of thermal fields, has not been captured except for short range between $42 > y^+ > 32$ at $Gr$ of $9.6\times10^5$. Further decrement of $Pr_\tau$ has been observed away from the wall for all studied here. Plots of other orientations of buoyant channel flows are shown in the same figure. Only at the opposing flow in the streamwise oriented buoyant channel flow [8], $Pr_\tau$ is the closest to that of non-buoyant case. At the aiding flow, $Pr_\tau$ is drastically decreasing. Turbulent Prandtl number in unstable stratification [9] matches the non-buoyant profile in the viscous sublayer but deviates from it and decreases steeply as $y^+$ increases. The blank portion in appeared unstable stratification profile in the range $53 > y^+ > 68$ is removed for clarity since it shows sharp oscillations due to the zero mean velocity gradient occurring in that range.

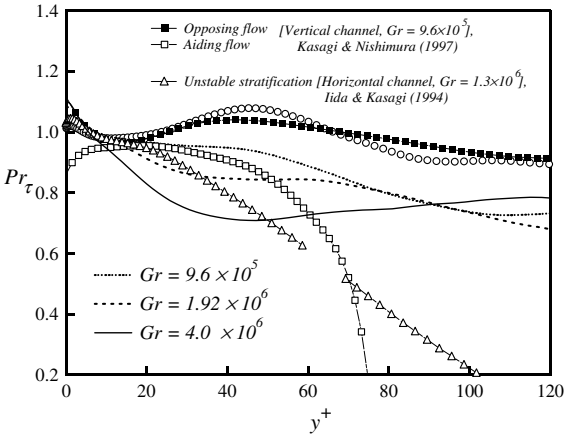


Fig. 10. Turbulent Prandtl number $Pr_\tau$ for different buoyant channel flows. Circles refer to plane channel flow of Iida et al. [10].

### 3.4. Budgets of Reynolds stresses

Using the transport equation of the Reynolds stresses and looking at the corresponding budgets of the each individual stress, one can explore the contribution of the different physical mechanisms affecting the Reynolds stresses under the buoyancy influence. The direct effect of buoyancy through the explicit production term can be traced alongside the indirect effects through the different diffusion and pressure velocity correlation mechanisms listed in Eq. (4). Comparisons are made between data obtained at the highest $Gr$ considered in the present study and those of non-buoyant channel flow of Iida et al. [10] in order to emphasis the changes made by buoyancy forces.

$$\underbrace{-\overline{u_i'^+v'^+}\frac{dU_i^+}{dy^+} - \overline{u_j'^+v'^+}\frac{dU_j^+}{dy^+}}_{\text{Mean production}} \underbrace{-\frac{Gr}{8Re_\tau^2}\left(\delta_{i3}\overline{u_j'^+\theta'^+} + \delta_{j3}\overline{u_i'^+\theta'^+}\right)}_{\text{Buoyancy production}} \underbrace{-\left(\overline{u_j^+\frac{\partial p'^+}{\partial x_i^+}} + \overline{u_i^+\frac{\partial p'^+}{\partial x_j^+}}\right)}_{\text{Velcoity–Pressure Gradient correlation}}$$
$$\underbrace{-\frac{\partial}{\partial y^+}\overline{u_i'^+u_j'^+v'^+}}_{\text{Turbulent diffusion}} + \underbrace{\frac{\partial^2}{\partial y^{+2}}\overline{u_i'^+u_j'^+}}_{\text{Viscous diffusion}} \underbrace{-2\overline{\frac{\partial u_i'^+}{\partial x_k^+}\frac{\partial u_j'^+}{\partial x_k^+}}}_{\text{Dissipation}} = 0 \qquad (4)$$

For $\overline{u'^+u'^+}$ budgets, the reduction of the mean production $-2\overline{u'^+v'^+}\,dU^+/dy^+$ is clear in region between $10 < y^+ < 80$ mainly due to the substantial decrease of $-\overline{u'^+v'^+}$, which is balanced by the decrease in dissipation as shown in Fig. 11(a). In the buffer region, while both turbulent diffusion and viscous diffusion decrease with

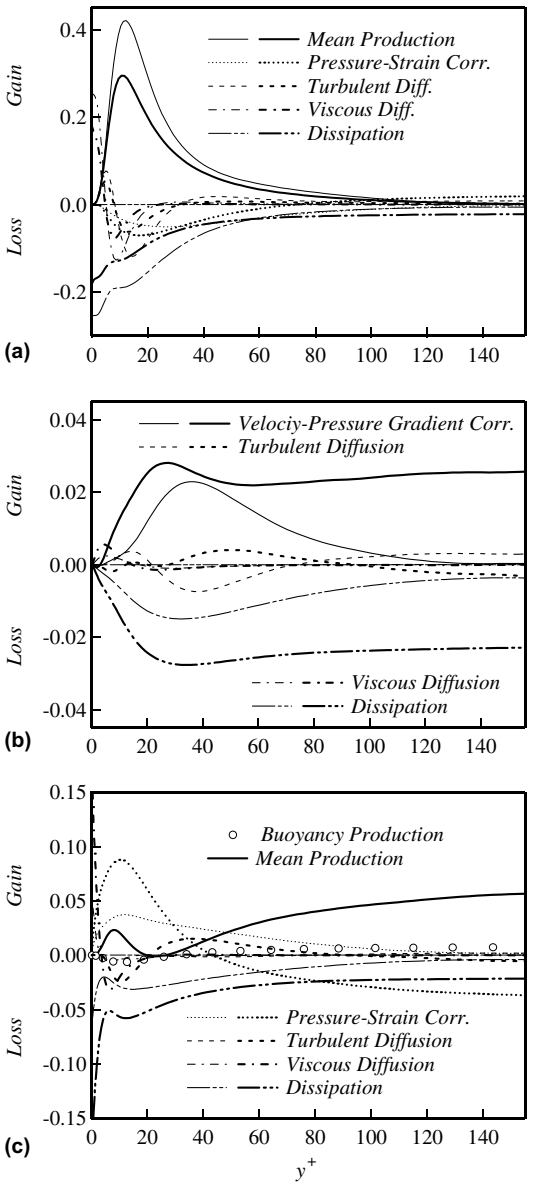


Fig. 11. Budgets of the normal Reynolds stresses: (a) $\overline{u'^+u'^+}$, (b) $\overline{v'^+v'^+}$, (c) $\overline{w'^+w'^+}$. Thick lines and circles for $Gr = 4.0 \times 10^6$. Thin lines non-buoyant flow of Iida et al. [10].

increasing $Gr$, pressure–strain correlation increases and works to suppress $\overline{u'^+u'^+}$. The enhancement of $\overline{u'^+u'^+}$ in the core of the channel observed in Fig. 4(a) can be attributed to the increase in pressure–strain correlation shown in Fig. 11(a).

The budgets of $\overline{v'^+v'^+}$ shows substantial changes even though no explicit term for the buoyancy exists in the transport equation. As shown in Fig. 11(b), the main contribution to the generation of $\overline{v'^+v'^+}$ at $y^+ < 20$ is the pressure diffusion. The pressure–strain correlation becomes the dominant term at $y^+ > 20$ whereas its role is minor in non-buoyant flow in the core region of the channel. The turbulent diffusion has small contribution in the budgets and it works to enhance $\overline{v'^+v'^+}$ in the buffer region and suppress it in the core region. The role of the turbulent diffusion at the highest $Gr$ case seems opposite to that in non-buoyant flow as shown in Fig. 11(b).

There are two major contributors in the budget of $\overline{w'^+w'^+}$ with the application of the buoyancy forces; the mean production due to the non-zero $dW/dy$ and the explicit term of the buoyancy production $Gr/4Re_\tau^2\overline{w'^+\theta'^+}$ as can be read in Eq. (4). The mean production $-2\overline{w'^+v'^+}\,dW^+/dy^+$ has a small peak in near-wall region as shown in Fig. 11(c) corresponding to the peak of $\overline{v'^+w'^+}$ observed in Fig. 5. It becomes the major contributor to $\overline{w'^+w'^+}$ at $y^+ > 40$ with a large peak at the channel centerline due to the maximum $\overline{v'^+w'^+}$ and $dW^+/dy^+$ attained there. Although the buoyancy production appears small in the range of $Gr$ studied here, it works to suppress the generation $\overline{w'^+w'^+}$ in near-wall region but to enhance it in the core region. The change of sign of the buoyancy production is reflected from the sign change of $\overline{w'^+\theta'^+}$. In buffer region, the main contributor to generating $\overline{w'^+w'^+}$ is the pressure–strain correlation. Since the sum of the pressure–strain correlations of the three normal stresses should be zero, by looking to those terms in Fig. 11(a)–(c) it can be observed that the energy is transferred from $\overline{u'^+u'^+}$ and $\overline{v'^+v'^+}$ to $\overline{w'^+w'^+}$ in the near wall-region at $y^+ < 20$, and only from $\overline{u'^+u'^+}$ to the other components in the region $20 < y^+ < 40$. Away from the wall, $y^+ > 40$, the mechanism is changed, thus energy is transferred from $\overline{w'^+w'^+}$ to $\overline{u'^+u'^+}$ and $\overline{w'^+w'^+}$.

Hence, the redistribution of energy through the pressure strain correlation at the highest $Gr$ differs from that of non-buoyant flows where $\overline{w'^+w'^+}$ drains energy from $\overline{u'^+u'^+}$ component further away from the wall. Turbulent diffusion shows also significant changes compared with non-buoyant flows, implying the necessity to better turbulence models to predict it. It can be also deduced from the budgets of the normal stresses that modeling the turbulent kinetic energy should consider carefully the turbulent and pressure diffusions.

Fig. 12(a) shows the budgets of the primary Reynolds shear stress $-\overline{u'^+v'^+}$. The mean production increases in the buffer layer mainly due to the enhancement of $\overline{v'^+v'^+}$. The turbulent diffusion is reduced in the buffer layer and the combined effect of the mean production and reduction of turbulent diffusion is to increase rather than to decrease $-\overline{u'^+v'^+}$. However, the substantial reduction in $-\overline{u'^+v'^+}$ shown previously in Fig. 5 is attributed to the considerable increase of the velocity-pressure gradient correlation, which overwhelms the two mechanisms mentioned above.

The budgets of the secondary Reynolds shear stress $-\overline{w'^+v'^+}$ is shown in Fig. 12(b) and the direct role of

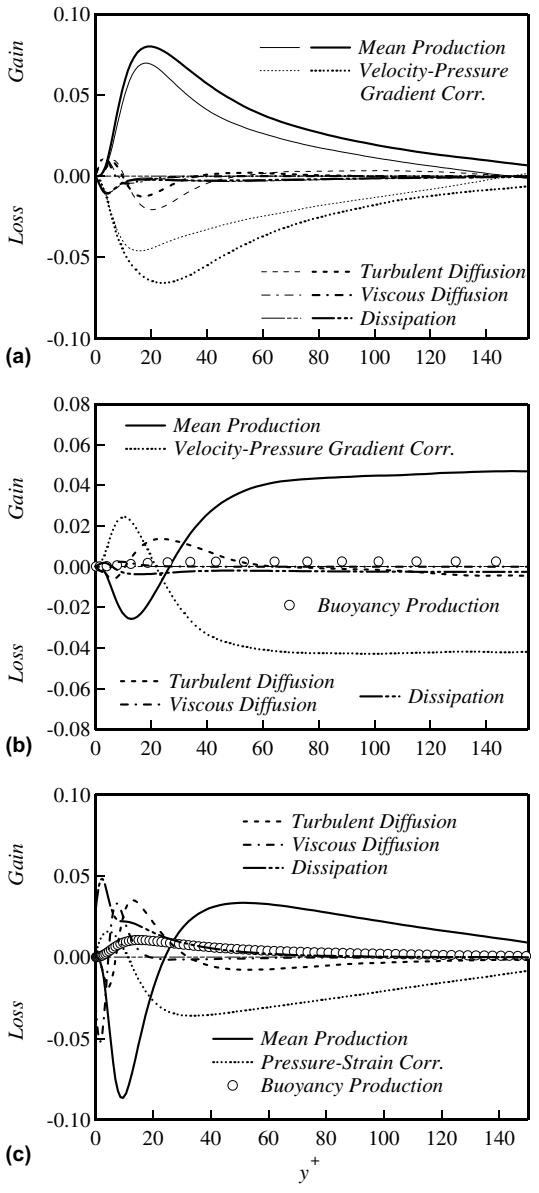


Fig. 12. Budgets of the off-diagonal Reynolds stresses: (a) $-\overline{u'^+u'^+}$, (b) $-\overline{w'^+v'^+}$, (c) $\overline{u'^+w'^+}$. Thick lines and circle for $Gr = 4.0 \times 10^6$. Thin lines non-buoyant flow of Iida et al. [10].

buoyancy can be withdrawn from Eq. (4) through the explicit term $Gr/8Re_\tau^2\overline{v'^+\theta'^+}$. Compared with the other terms, the effect of the buoyancy production is relatively small. However, it enhances $-\overline{w'^+v'^+}$ from wall to the centerline of the channel since $\overline{v'^+\theta'^+}$ does not change sign within the channel depth. In near wall region, the velocity-pressure gradient correlation balances the mean production. For $10 < y^+ < 50$, the turbulent diffusion becomes significant. In particular, the velocity-pressure gradient and turbulent diffusion work together against the generation of $-\overline{w'^+v'^+}$ in near-wall region, which is reflected in the stationary profiles of $-\overline{w'^+v'^+}$ stress observed in Fig. 5.

The significant direct effect of buoyancy can be seen in budgets of the third Reynolds stress $\overline{u'^+w'^+}$ where the buoyancy production is of comparable to the other terms in the budgets as shown in Fig. 12(c). In this figure, it can be seen that the viscous and turbulent diffusion have important contribution in the buffer region

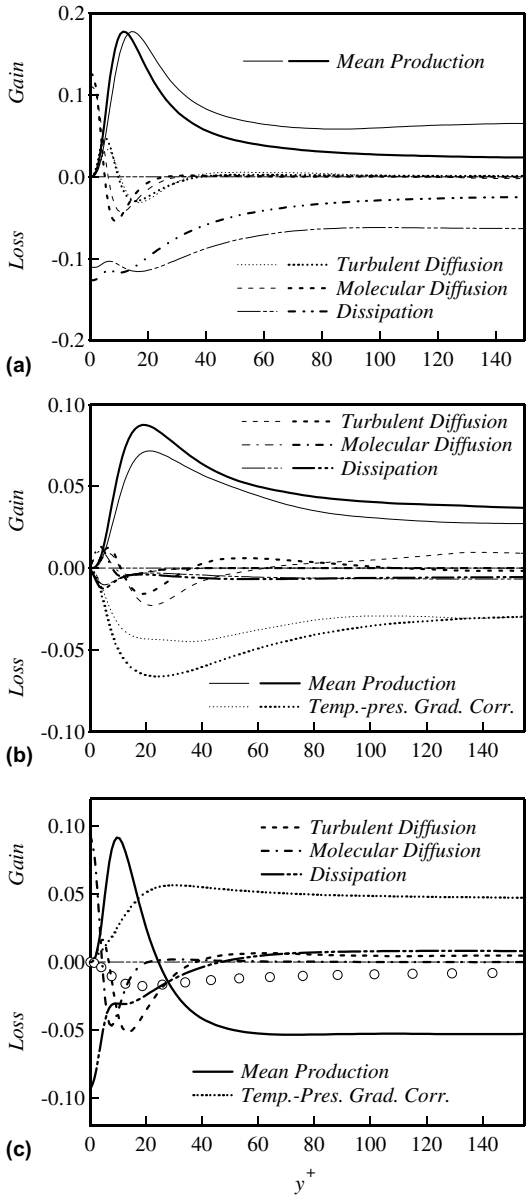


Fig. 13. Budgets of temperature variance and turbulent heat fluxes: (a) $\overline{\theta'^{+2}}$, (b) $\overline{v'^+\theta'^+}$, (c) $\overline{w'^+\theta'^+}$. Thick lines and circles for $Gr = 4.0 \times 10^6$. Thin lines non-buoyant flow of Iida et al. [10].

in contrast to the diffusion terms of the other off-diagonal stresses. Away from the wall, the pressure–strain correlation has dominant effect and it balances the mean production although its role at $y^+ < 10$ is relatively small compared by the other terms.

### 3.5. Budgets of temperature variance and turbulent heat fluxes

Equation (5) lists the different terms of the temperature variance $\theta'^{+2}$ transport equation and its budgets is plotted in Fig. 13(a) for the highest $Gr$ in comparison with the non-buoyant channel flow of Iida et al. [10].

$$\underbrace{-2\overline{v'^+\theta'^+}\frac{\mathrm{d}\Theta^+}{\mathrm{d}y^+}}_{\text{Mean production}} \quad \underbrace{-\frac{\partial}{\partial y^+}\overline{v'^+v'^+\theta'^+}}_{\text{Turbulent diffusion}} + \underbrace{\frac{1}{Pr}\frac{\partial^2\overline{\theta'^{+2}}}{\partial y^{+2}}}_{\text{Molecular diffusion}} \quad \underbrace{-\frac{2}{Pr}\overline{\frac{\partial\theta'^+}{\partial x_k^+}\frac{\partial\theta'^+}{\partial x_k^+}}}_{\text{Dissipation}} = 0. \tag{5}$$

The significant changes can be seen in the reduction of the mean production term due to the decrease of $\mathrm{d}\Theta/\mathrm{d}y$ observed in Fig. 3 especially at $y^+ > 20$. In near-wall region, minor changes in the molecular and turbulent diffusion terms can be seen whereas the dissipation increases in the vicinity of the wall.

The transport equation for the turbulent heat flux is:

$$\underbrace{-\overline{v'^+\theta'^+}\frac{\mathrm{d}U_i^+}{\mathrm{d}y^+} - \overline{u_i'^+v'^+}\frac{\mathrm{d}\Theta^+}{\mathrm{d}y^+}}_{\text{Mean production}} \quad \underbrace{-\delta_{i3}\frac{Gr}{8Re_\tau^2}\overline{\theta'^+\theta'^+}}_{\text{Buoyancy production}} + \underbrace{\overline{\theta'^+\frac{\partial p'^+}{\partial x_i^+}}}_{\text{Temperature–Pressure Gradient correlation}}$$

$$\underbrace{-\frac{\partial}{\partial y^+}\overline{u_i'^+v'^+\theta'^+}}_{\text{Turbulent Diffusion}} + \underbrace{\frac{\partial}{\partial y^+}\left(\overline{\theta'\frac{\partial u_i'^+}{\partial y^+}} + \frac{1}{Pr}\overline{u_i'^+\frac{\partial\theta'^+}{\partial y^+}}\right)}_{\text{Molecular Diffusion}} \quad \underbrace{-\left(1+\frac{1}{Pr}\right)\overline{\frac{\partial u_i'^+}{\partial x_k^+}\frac{\partial\theta'^+}{\partial x_k^+}}}_{\text{Dissipation}} = 0 \tag{6}$$

The effect of buoyancy on the budgets of the two transverse components of the turbulent heat fluxes show major changes compared with the streamwise heat flux which is omitted for brevity. The budget of the wall-normal heat flux $\overline{v'^+\theta'^+}$ is plotted in Fig. 13(b). The mean production increases in the near-wall region due to the substantial increase of $\mathrm{d}\Theta/\mathrm{d}y$ and in the log-law and wake regions due to the increase of $\overline{v'^+v'^+}$. The increase in the mean production is met by considerable increase in temperature-pressure gradient correlation. At $40 > y^+ > 20$ turbulent diffusion decreases aiding to increase $\overline{v'^+\theta'^+}$ and at $40 > y^+$ it shows slight increase and then becomes smaller at the core region. However, at $y^+ < 20$, minor changes in the diffusion and dissipation terms can be seen in Fig. 13(b).

The importance of the third turbulent heat flux comes in being one of the production terms of $\overline{w'^+w'^+}$. Among the three components of turbulent heat fluxes, the direct effect of buoyancy appears only in $\overline{w'^+\theta'^+}$ through the term $Gr/8Re_\tau^2\theta'^{+2}$ which is of the same order of the other terms in the budgets at the highest $Gr$ as shown in Fig. 13(c). Referring to Fig. 9(d), the peak of $\overline{w'^+\theta'^+}$ profiles seems unchanged when $Gr$ increases from $1.92\times10^6$ to $4.0\times10^6$ which can be attributed to the growth of the buoyancy production term against the mean production of $\overline{w'^+\theta'^+}$ in near-wall region. However, the buoyancy production works to enhance $\overline{w'^+\theta'^+}$ in the log-law region. In general, all the terms in the budgets are significant except the molecular diffusion at $y^+ > 20$. The temperature-pressure gradient correlation is positive and dominant contributor within the channel depth. This indicates the prevailing of large eddies which rotate in the same sense of the mean spanwise gradient which will be explained later using the cross-section visualization.

### 3.6. Flow visualizations

In this section, the effect of buoyancy on the flow and thermal fields is investigated by looking at the instantaneous fields at different horizontal and vertical planes. The low- and high-speed streaks and the corresponding thermal streaks taken at same distance around $y^+ \sim 10$ near the cold wall are presented in Fig. 14(a)–(c) for the three Grashof numbers. The increased titling of the low- and high-speed and thermal streaks towards the positive $z$-direction is clearly observed with increasing $Gr$ due to the increase of $W$. The longitudinal length of the streaks decreases and the streaks meandering illustrates high irregularity which is more pronounced at the highest $Gr$ as shown in Fig. 14(c). The similarity between low- and high-speed streaks and the thermal streaks is still observed at the lowest $Gr$. However, it becomes weaker at the highest $Gr$, where spots of high or low streamwise velocity fluctuations do not concur exactly with those of high or low temperature fluctuations as shown in Fig. 14(c). This indicates that the mechanisms of momentum and heat transport are different

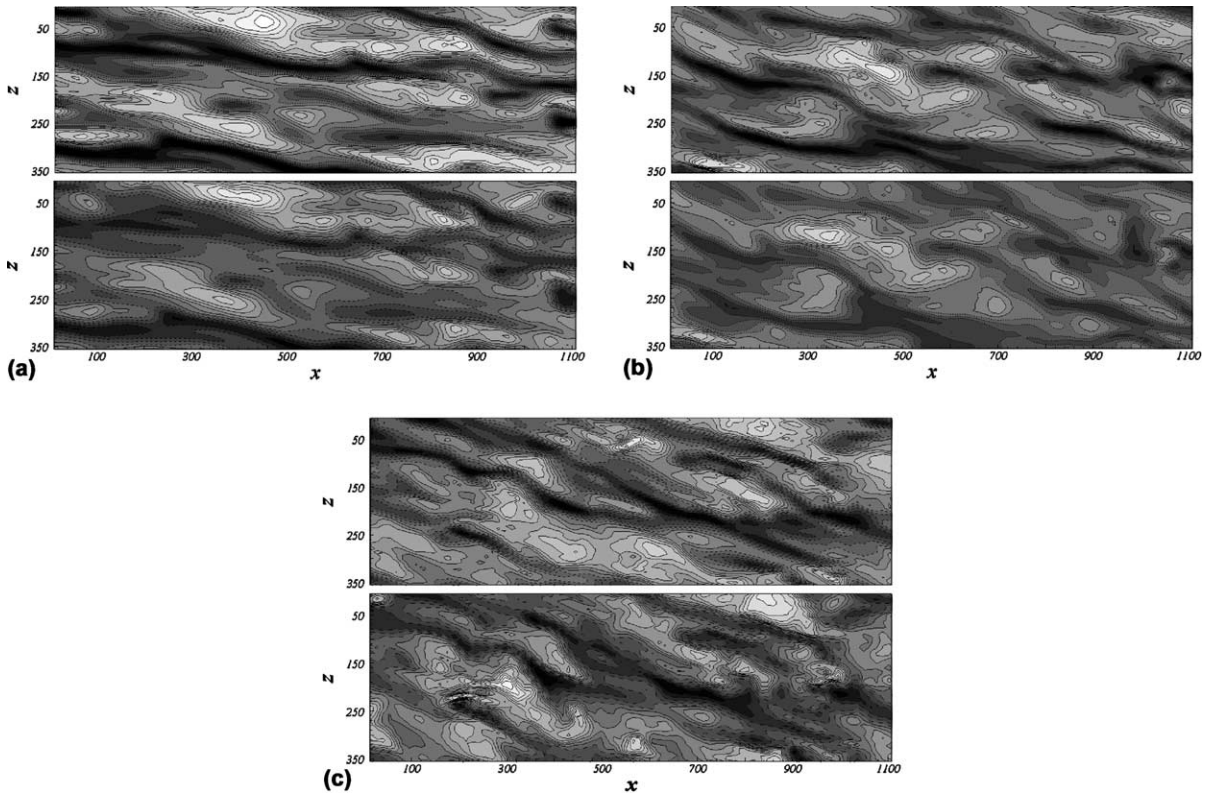


Fig. 14. Streaky structures near the cold wall at $y^+ = 13$: (a) $Gr = 9.6 \times 10^5$, (b) $Gr = 1.92 \times 10^6$, (c) $Gr = 4.0 \times 10^6$. Upper figure is the low- and high-speed streaks; lower figure is the thermal streaks. White to black is positive to negative fluctuations with 20 contour levels.

under the effect of buoyancy in accordance to the decrease in the correlation coefficient of $u'$ and $\theta'$ than that of non-buoyant flow as shown in Fig. 15.

Spanwise two-point correlations of the streamwise velocity fluctuations are shown in Fig. 16(a) for the three

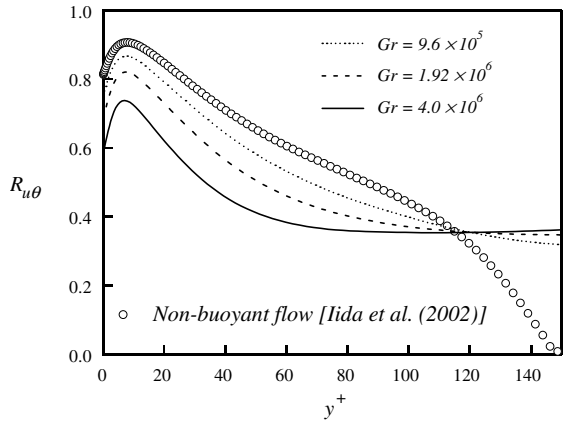


Fig. 15. The correlation coefficients $R_{u\theta}$.

$Gr$ compared with the plane channel flow of Kim et al. [17]. The strong negative correlation occurs at around $r_z^+ \sim 52.6$ in plane channel, and it becomes weaker with increasing $Gr$ from $9.6 \times 10^5$ to $1.92 \times 10^6$ giving separation of 52.0 and 53.7 for both low and moderate $Gr$, respectively, which are in agreement of typical streaks spacing of turbulent boundary layers. However, increasing $Gr$ further to $4.0 \times 10^6$ results in weaker correlation with nearly constant value for wide range of separation ($50 < r_z^+ < 100$) where the weak minimum correlation occurs at $r_z^+ \sim 64.6$. The weak $R_{uu}$ indicates that the streaks have no preference spacing at the highest $Gr$ although the spacing in general increases. The increase of streaks spacing can be related to the changes of near-wall vortical structures which appear to be asymmetry and larger in size.

In Fig. 16(b), the minimum correlations of $R_{vv}$ range from $r_z^+ \sim 29$ in plane channel flow to around 32.3 in the highest $Gr$. As explained by Kim et al. [17], the minimum of $R_{vv}$ is a measure of the vortical structure diameter which seems to increase with increasing $Gr$. Moreover, $R_{vv}$ stays negative for larger $r_z^+$ which indicates the existence of eddies of larger size in near wall region.

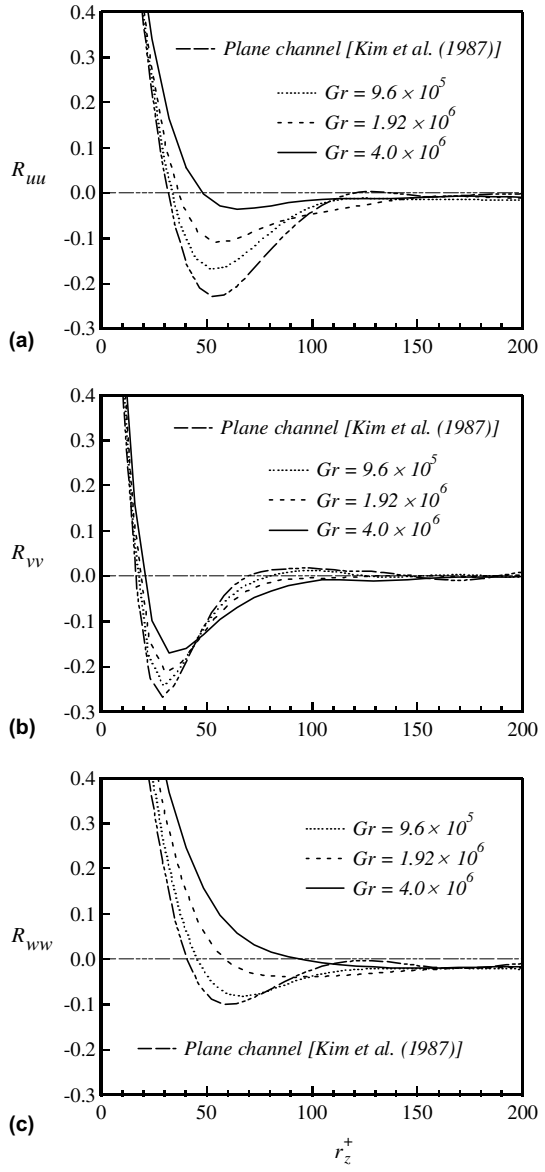


Fig. 16. Two-point correlations at $y^+ \sim 10$: (a) $R_{uu}$, (b) $R_{vv}$, (c) $R_{ww}$.

The minimum of $R_{ww}$ in plane channel flow can be a measure of the distance between centers of counter rotating vortical structures or it can be a consequence of the impingement effect cause by single vortex inducing two opposite streams of $w'$ likely to be of the same strength. Such minimum occurs at around 59 wall units in plane channel flow [17]. It is shown in Fig. 16(c) that $R_{ww}$ at the lowest $Gr$ is similar to the plane channel flow whereas it becomes weak and its minimum occurs at higher $r_z^+$ with increasing $Gr$. This implies that the spacing between the counter-rotating vortices increases and their strength becomes asymmetric where one of the vortices is boosted (which has the same sign as that of $\mathrm{d}W/\mathrm{d}y$) and the other is reduced in size. The asymmetric distribution of the counter rotating vortices is similar to that observed in the turbulent channel subjected to streamwise rotation, in which anti-symmetric profile of $W$ was also attained and the streaks spacing was observed to be higher than that of plane channel flow [22]. The trend observed in $R_{ww}$ can also reflect the existence of large eddies in near wall region resulting from the emerging of thermal plumes where their spacing is quite wide in the spanwise direction.

Cross-stream velocity vectors and contours of temperature fluctuations averaged over three successive $z$–$y$ planes, in order to maintain the coherent structure, are plotted in Fig. 17 for the lowest and highest $Gr$. Averaging over more planes smeared the structures due to the titling of the flow direction. In Fig. 17(a), the lowest $Gr$ shows similarity with plane channel flow where several pairs of counter rotating vortices can be identified. Larger eddies can be also observed. The contours of temperature fluctuations illustrate the thermal streaks corresponding to the different vortices which appear as successive positive and negative spots with spacing around 100 wall units near each wall. At the highest $Gr$ shown in Fig. 17(b), the number of counter rotating vortices is reduced and larger eddies become more frequent with no clear preference for the streaks spacing. On the other hand, temperature contours show large thermal plumes associated with the large eddies observed in the velocity vectors. The symmetry of counter-rotating vortices and the emerging of large eddies rotating in the same sense of that of $\mathrm{d}W/\mathrm{d}y$ dominate the oppositely rotating vortices. The dominant vortices carry positive/negative $\theta'$ from the heated/cooled wall to the channel core and bring negative/positive $\theta'$ from the core region towards the heated/called wall. Hence they produce negative $\mathrm{d}\theta'/\mathrm{d}y$ across the eddy as depicted by eddies E1 and E2 in Fig. 17(b). Since the pressure is negative inside the eddies, the dominance of large eddies explains the positive profile of temperature-pressure gradient correlation in the budgets of $\overline{w'^{+}\theta'^{+}}$ as shown in Fig. 13(c).

Spanwise power spectra for streamwise velocity and temperature fluctuations at $y^+ \sim 10$ are plotted in Fig. 18. The spectra increase at low wave numbers with increasing $Gr$ due to the thermal plumes emerged in near-wall region generating large eddies in near-wall region. Meanwhile the spectra decrease significantly with increasing $Gr$ at moderate wave numbers which include the streaks spacing. This indicates that the attenuation of mechanism of generating and sustaining the typical coherent structures observed in plane channel.

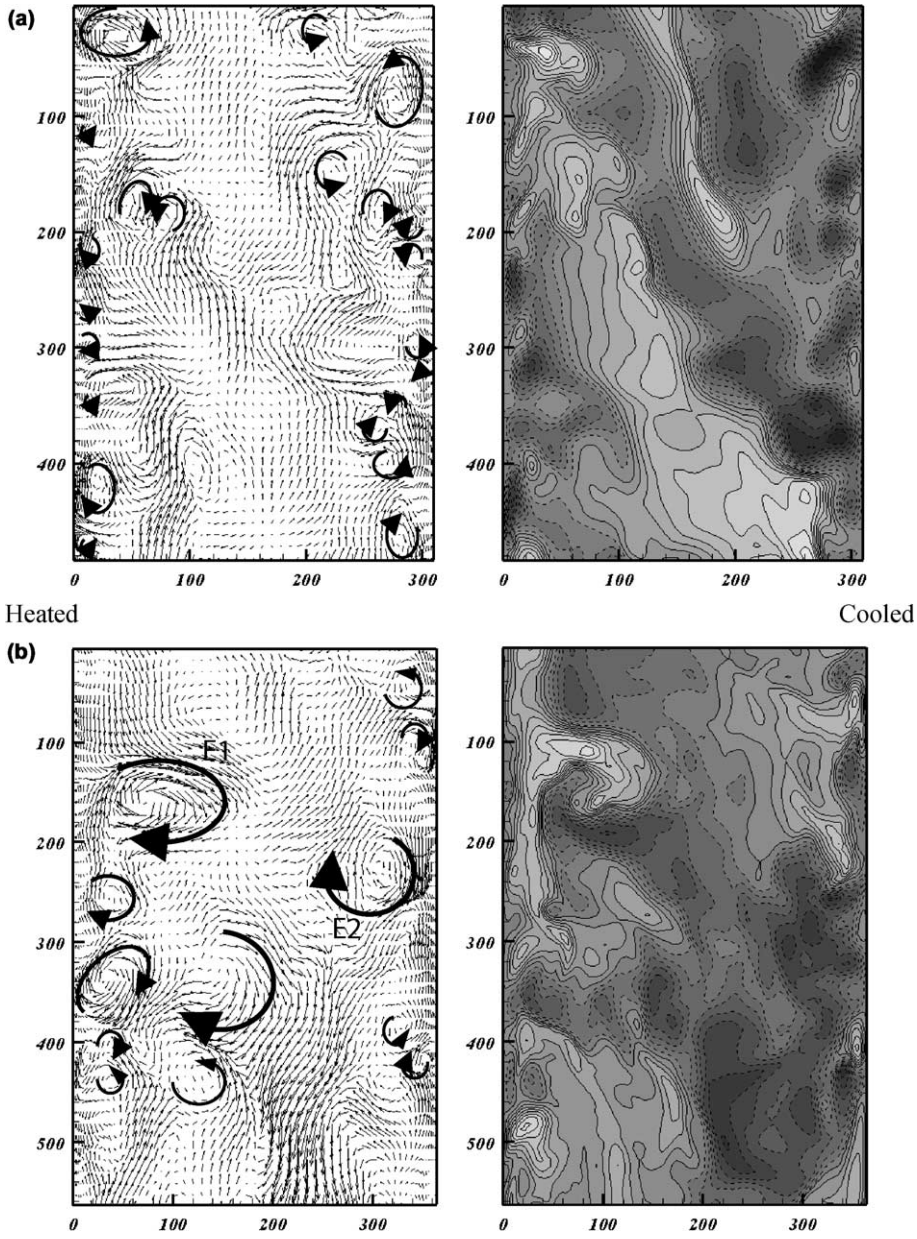


Fig. 17. Cross-stream planes of temperature fluctuations contours and secondary flow vectors: (a) $Gr = 9.6 \times 10^5$, (b) $Gr = 4.0 \times 10^6$. White to black refers to positive to negative temperature fluctuations with 20 contour levels. Dashed lines are contours of negative temperature fluctuations.

## 4. Conclusions

The present study aims at exploring the effects of buoyancy when it is aligned in the normal to the mean flow direction in planes parallel to the bounding walls. The innovation of the present work is the initiation of three-dimensional turbulent boundary layer with the mean spanwise strain is high near the wall and non-zero further away from the wall. Such newly generated strain is responsible for activating turbulence intensities especially in the core of the channel.

The features of the 3DTBL flows have been captured where significant reduction of the primary Reynolds shear stress and the structure parameter $a_1$ are attained.

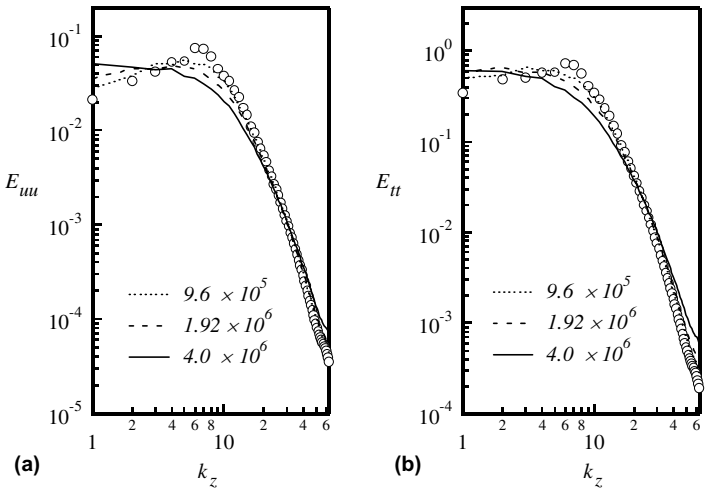


Fig. 18. Spanwise power spectra at $y^+ \sim 10$: (a) streamwise velocity fluctuations, (b) temperature fluctuations. Circles refer to plane channel flow of Iida et al. [10].

However, the heat transfer mechanism differs from that of momentum transfer where enhancement of the wall-normal turbulent heat flux is observed in contrast to the reduction of the primary Reynolds stress. The study addresses the difficulty of modeling the resulting buoyant flow. The ambiguity of assuming the isotropy eddy viscosity due to the large lag angle between shear stress and velocity gradient vectors and the substantial changes of turbulent Prandtl number emphasis such difficulty.

Detailed budgets of the transport equations of Reynolds stresses and turbulent heat fluxes are presented. Although the direct effect of buoyancy through the explicit production term is small at this range of Grashof numbers, the pressure gradient correlations are shown to be drastically changing. The turbulent diffusion terms are also of importance in this particular flow. Such budgets are believed to important for turbulence modelers to testify and improve models dealing with buoyancy.

Flow visualizations indicate the tilting of the streaky structures whose longitudinal lengths become shorter. With increasing Grashof number, the typical counter rotating vortices become asymmetry. Eddies associated with thermal plumes are also observed and their roles in the temperature-pressure gradient correlation is explained. Further investigations are needed to deepen out understanding for the dissimilarity between momentum and heat transfer observed in this particular flow highlighting the influence of the observed changes of turbulent structures on both mechanisms.

Higher Reynolds number simulations are considered to explorer the dependency of the current observation on Reynolds number. Inclined surfaces to the gravity vector seem interesting for future simulations.

## Acknowledgments

The authors are grateful to Professor Jong Chun Park for his helpful discussion and assistance in using the computational facilities. This work was supported by Advanced Ship Engineering Research Center (ASERC), Pusan National University, through the Korean Science and Engineering Foundation.

## References

[1] J.R. Phillips, Direct simulations of turbulent unstratified natural convection in a vertical slot for $Pr = 0.71$, Int. J. Mass Heat Transfer 39 (1996) 2485–2494.

[2] R. Boudjemadi, V. Maupu, D. Laurence, P.Le. Quéré, Budgets of turbulent stresses and fluxes in a vertical slot natural convection flow at Rayleigh $Ra = 10^5$ and $5.4 \times 10^5$, Int. J. Heat Fluid Flow 18 (1997) 70–79.

[3] T.A.M. Versteegh, F.T.M. Nieuwstadt, Turbulent budgets of natural convection in an infinite, differentially, heated, vertical channel, Int. J. Heat Fluid Flow 19 (1998) 135–149.

[4] T.A.M. Versteegh, F.T.M. Nieuwstadt, A direct numerical simulation of natural convection between two infinite vertical differentially heated walls: scaling laws and wall functions, Int. J. Mass Heat Transfer 42 (1999) 3673–3693.

[5] M. Wang, S. Fu, G. Zhang, Large-scale spiral structures in turbulent thermal convection between two vertical plates, Phys. Rev. E 66 (2002) 066306.

[6] M. Wörner, G. Grötzbach, Pressure transport in direct numerical simulations of turbulent natural convection in

horizontal fluid layers, Int. J. Heat Fluid Flow 19 (1998) 150–158.
[7] J.A. Domaradzki, P.W. Metcalfe, Direct numerical simulations of the effects of shear on turbulent Rayleigh–Bénard convection, J. Fluid Mech. 193 (1988) 499–531.
[8] N. Kasagi, M. Nishimura, Direct numerical simulation of combined forced and natural turbulent convection in a vertical plane channel, Int. J. Heat Fluid Flow 18 (1997) 88–99.
[9] O. Iida, N. Kasagi, Direct numerical simulation of unstably stratified turbulent channel flow, ASME Trans. Heat Transfer 119 (1997) 53–61.
[10] O. Iida, N. Kasagi, Y. Nagano, Direct numerical simulation of turbulent channel flow under stably density stratification, Int. J. Mass Heat Transfer 45 (2002) 1693–1703.
[11] H.S. Dol, K. Hanjalić, S. Kenjereš, A comparative assessment of the second-moment differential and algebraic models in turbulent natural convection, Int. J. Heat Fluid Flow 18 (1997) 4–14.
[12] T.P. Sommer, R.M.C. So, Wall-bounded buoyant turbulent flow and its modeling, Int. J. Mass Heat Transfer 39 (1996) 3595–3606.
[13] S.S. Girimaji, S. Balachandar, Analysis and modeling of buoyancy-generated turbulence using numerical data, Int. J. Mass Heat Transfer 4 (1998) 915–929.
[14] H.S. Dol, K. Hanjalić, T.A.M. Versteegh, A DNS-based thermal second-moment closure for buoyant convection at vertical walls, J. Fluid Mech. 391 (1999) 211–247.
[15] I. Tiselj, E. Pogrebnyak, C. Li, A. Mosyak, G. Hetsroni, Effect of wall boundary condition on scalar transfer in a fully developed turbulent flame, Phys. Fluids 13 (2001) 1028–1039.
[16] Y. Seki, H. Abe, H. Kawamura, DNS of turbulent heat transfer in a channel flow with different thermal boundary conditions, The 6th ASME-JSME Thermal Engineering Joint Conference, 2003.
[17] J. Kim, P. Moin, R. Moser, Turbulence statistics in fully developed channel flow at low Reynolds number, J. Fluid Mech. 177 (1987) 133–166.
[18] O. El-Samni, Heat and momentum transfer in rotating channel flow, Ph.D. thesis, The University of Tokyo, Japan, 2001.
[19] D.A. Compton, J.K. Eaton, Near-wall measurements in a three-dimensional turbulent boundary layer, J. Fluid Mech. 350 (1997) 189–208.
[20] J.K. Eaton, Effects of mean flow three dimensionality on turbulent boundary-layer structure, AIAA J. 33 (1995) 2020–2025.
[21] P. Moin, T.-H. Shih, D. Driver, N.N. Mansour, Direct numerical simulation of a three-dimensional turbulent boundary layer, Phys. Fluids A 2 (1990) 1846–1853.
[22] O. El-Samni, N. Kasagi, The effects of system rotation with three orthogonal rotating axes on turbulent channel flow, in: Proceeding of the 7th International Congress on Fluid Dynamics and Propulsion, Cairo, Egypt, December 18–20, 2001, CD-ROM.